

Neutron sensitivity of ${}^6\text{Li}$ -based suspended foil microstrip neutron detectors using Schott Borofloat® 33 microstrip electrodes

Nathaniel S. Edwards^{a,*}, Benjamin W. Montag^{a,b}, Luke C. Henson^b, Steven L. Bellinger^{a,b}, Daniel M. Nichols^a, Michael A. Reichenberger^a, Ryan G. Fronk^a, Douglas S. McGregor^a

^a S.M.A.R.T. Laboratory, Department of Mechanical and Nuclear Engineering, Kansas State University, Manhattan, KS 66506, USA

^b Radiation Detection Technologies, Inc., Manhattan, KS 66502, USA

ARTICLE INFO

Keywords:

${}^3\text{He}$ alternative
Neutron detection
Microstrip electrodes
Lithium foil
Radiation detector characterization

ABSTRACT

${}^6\text{Li}$ foils, each 75- μm thick, were positioned between a Schott Borofloat® 33 microstrip electrode and a planar drift electrode to construct suspended foil microstrip neutron detectors. MCNP6 simulations of two detector configurations, one containing a single ${}^6\text{Li}$ foil and the other containing five ${}^6\text{Li}$ foils, indicated expected maximum intrinsic thermal-neutron detection efficiencies of 18.36% and 54.08%, respectively. For comparison, the intrinsic thermal-neutron detection efficiency as a function of thermal-neutron beam position along the foil span was experimentally measured for both detector configurations. A non-uniform intrinsic thermal-neutron detection efficiency distribution was observed along the span of the ${}^6\text{Li}$ foil(s) between the microstrip and drift electrodes. Maximum intrinsic thermal-neutron detection efficiencies of $12.58 \pm 0.15\%$ and $29.75 \pm 0.26\%$ for the single and five ${}^6\text{Li}$ foils were measured, respectively. Gamma-ray rejection ratios of $6.46 \times 10^{-5} \pm 4.32 \times 10^{-7}$ and $7.96 \times 10^{-5} \pm 4.65 \times 10^{-7}$ were also measured, respectively, for a ${}^{137}\text{Cs}$ exposure rate of 50 mR h^{-1} . All measurements were conducted with the ${}^6\text{Li}$ foil(s) contained within a sealed aluminum enclosure pressurized with 10 psig of P-10 gas.

1. Introduction

The ${}^3\text{He}$ supply shortage (Kouzes, 2009; Shea and Morgan, 2010), resulting in an increase in the cost of ${}^3\text{He}$, has motivated the development of several low-cost, high-efficiency, low-gamma-ray-sensitivity alternative technologies (Kouzes et al., 2010, 2015; Hurd and Kouzes, 2014). Multi-wire proportional counters (MWPC) with ${}^6\text{Li}$ -foils as neutron converters were previously developed as a ${}^3\text{He}$ -alternative technology and these detectors had high intrinsic thermal-neutron detection efficiencies, ϵ_{th} , and low sensitivity to gamma rays (Nelson et al., 2011, 2012, 2014a, 2014b, 2015; Nelson, 2013). Reducing the size of ${}^6\text{Li}$ -foil MWPCs is limited due to a minimum space needed between neighboring ${}^6\text{Li}$ foils for anode wires. Likewise, the anode wires are susceptible to mechanical vibrations that induce microphonic noise. Suspended foil microstrip neutron detectors (SFMND) were developed (Edwards et al., 2016) by replacing the anode wires with a microstrip electrode (Oed, 1988). These detectors maintain the high ϵ_{th} of suspended ${}^6\text{Li}$ foils with the mechanical and electrical capabilities of microstrip electrodes (Fig. 1). SFMNDs are under development with the goal of producing a robust, low-cost, and compact ${}^3\text{He}$ -alternative technology capable of achieving high ϵ_{th} while maintaining low

sensitivity to gamma rays.

Microstrip electrodes were previously utilized for a variety of neutron detection applications primarily relying on ${}^3\text{He}$ gas as the neutron conversion medium (Oed, 1988, 2004; Oed et al., 1989; Vellettaz et al., 1997; Clergeau et al., 2001; Takahashi et al., 2004; Fujita et al., 2007; Bateman et al., 2010, 2013). Studies were also performed using other neutron conversion media such as CsI-coated ${}^6\text{Li}$ and ${}^{157}\text{Gd}$ foils (Oed, 2004; Gebauer et al., 1998; Masaoka et al., 2003). However, bare ${}^6\text{Li}$ metals were not used because of the chemical reactivity of the material. ${}^6\text{Li}$ -based SFMNDs with one and five suspended 75- μm thick ${}^6\text{Li}$ foils using a silicon-based microstrip electrode were previously fabricated and tested (Edwards et al., 2016). Substantial differences between measured and simulated ϵ_{th} were observed, suspected to be due to microstrip electrode-based electrical phenomena (Edwards et al., 2016). Therefore, investigations into an electrically stable microstrip electrode substrate were conducted (Edwards et al., 2018). Schott Borofloat® 33 was identified as a low-cost, electrically stable microstrip electrode substrate that also reduced the capacitance from previously-used silicon-based microstrip electrodes (Edwards et al., 2018). The present work focuses on the optimization and refinement of ${}^6\text{Li}$ -based SFMNDs via the fabrication and neutron-sensitivity testing of ${}^6\text{Li}$ -based

* Corresponding author.

E-mail address: nedwards@ksu.edu (N.S. Edwards).

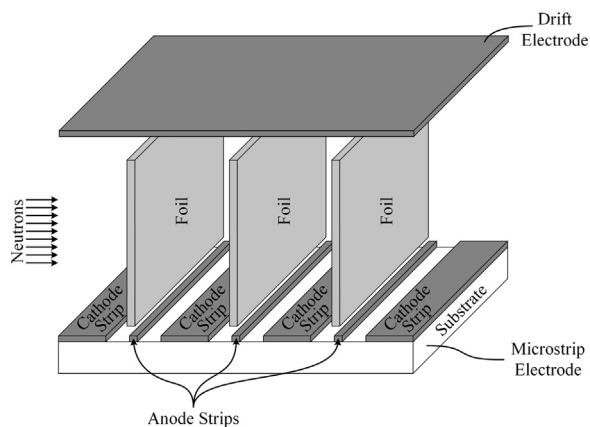
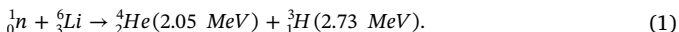


Fig. 1. Configuration of a SFMND depicting the orientation of suspended foils relative to microstrip and drift electrodes.

SFMNDs using a Schott Borofloat® 33 microstrip electrode.

2. Theoretical considerations

Neutron detection using the ⁶Li-based SFMND occurs in three main steps, as depicted in Fig. 2: 1.) neutron conversion, 2.) drift of charge carriers, and 3.) charge multiplication. The first step occurs when an incident slow neutron is absorbed by a ⁶Li atom with a microscopic thermal-neutron absorption cross-section of 940 b (Knoll, 2010; Tsoulfanidis, 1995; McGregor et al., 2003). The ensuing ⁶Li(n,α)³He reaction, with a total reaction Q-value of 4.78 MeV, yields reaction products that are emitted in opposite directions with energies described by,



Although the thermal-neutron absorption cross-section of ⁶Li is lower than ¹⁰B (3840 b) (Knoll, 2010; Tsoulfanidis, 1995; McGregor et al., 2003), the reaction Q-value is significantly higher than that of ¹⁰B (2.31 MeV). This increase in reaction Q-value allows for sufficient discrimination of background radiation and gamma rays without significantly sacrificing neutron-detection performance.

Upon exiting the ⁶Li foil and entering the backfill gas, the reaction products ionize the backfill gas resulting in the liberation of charge carriers. The second step in the detection process occurs when the potential difference between the drift electrode voltage, V_d , and the microstrip anode and cathode strip voltages, V_a and V_c , respectively, cause charge carriers to drift through the gas within the drift electric field. The operating voltage condition of $V_d < V_c < V_a$ is required to drift electrons towards the microstrip electrode surface and positively-charged ions towards the drift electrode. Therefore, the second step of the detection process is equivalent to the signal formation process that occurs in a parallel-plate ionization chamber. When electrons approach the microstrip electrode surface, the electric field strength increases by

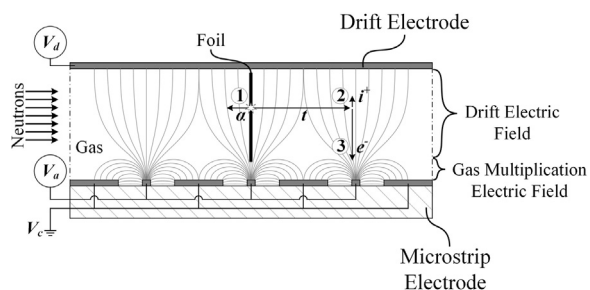


Fig. 2. Three-step neutron detection process for suspended ⁶Li foil(s) positioned between a drift electrode and a microstrip electrode.

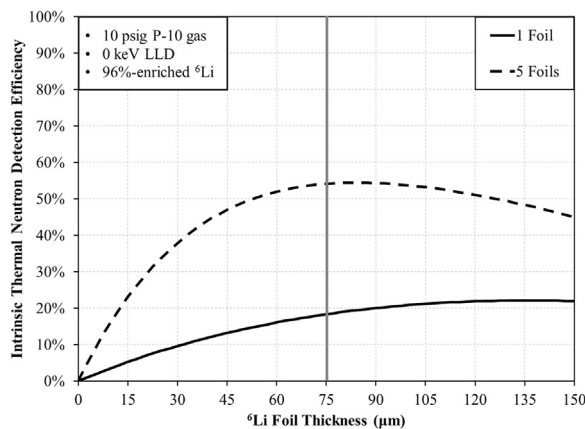


Fig. 3. MCNP6-simulated ϵ_{th} curves as a function of ⁶Li foil thickness for one and five foils in 10 psig (1.68 atm) of P-10 proportional gas. The foils were assumed to be 96%-enriched ⁶Li and the ϵ_{th} curves are plotted for a LLD setting of 0 keV.

several orders of magnitude and surpasses the critical electric field strength necessary to cause Townsend avalanching, denoted in Fig. 2 as the gas multiplication electric field region. This increase in electric-field strength occurs as a result of the potential difference between neighboring anode and cathode strips positioned less than 1.0 mm apart, where $V_a > V_c$. Furthermore, the difference in anode and cathode strip width provides a geometric weighting condition that further enhances the electric field strength beyond the potential difference between neighboring anode and cathode strips. Thus, the third step in the neutron detection process occurs at this electric-field boundary where gas multiplication can occur.

The ϵ_{th} as a function of ⁶Li foil thickness for SFMNDs containing one and five foils was simulated using MCNP6 as shown in Fig. 3. A lower level discriminator (LLD) setting of 0 keV was used when generating the ϵ_{th} curves to determine the maximum ϵ_{th} as a function of foil number and thickness. P-10 proportional gas (90% argon, 10% methane) pressurized to 10 psig (1.68 atm) was backfilled into a chamber with 96%-enriched ⁶Li foils. For 75-μm thick ⁶Li foils, theoretical ϵ_{th} of 18.36% and 54.08% are predicted for a chamber with one and five foils, respectively. Simulated reaction-product pulse-height spectra, corresponding to the left y-axis with units of “counts/source neutron”, for one and five ⁶Li foils are shown in Fig. 4. The simulated ϵ_{th} shown in Fig. 4, corresponding to the right ordinate, indicates the change in neutron-detection performance as a function of LLD setting. Thus, as the prominence of the simulated reaction-product spectral features increases, the simulated ϵ_{th} decreases.

The difference in pulse-height spectra features shown in Fig. 4 is a consequence of differences in foil positions coupled with differences in interaction location, reaction-product particle ranges, and their corresponding particle trajectories (Nelson, 2013; Nelson et al., 2014a). Four reaction-product emission scenarios exist, as previously reported in literature (Nelson, 2013; Nelson et al., 2014a), based on the range in pure ⁶Li foil of the 2.05 MeV alpha particles and 2.73 MeV tritons of 23.2 μm and 133 μm, respectively (Nelson, 2013; Nelson et al., 2014a; Ziegler and Biersack, 2013). The ranges of the 2.05 MeV alpha particle and 2.73 MeV triton are 7.50 mm and 43.2 mm, respectively, in 10 psig of P-10 proportional gas (Ziegler and Biersack, 2013). The single-foil scenario was simulated with the foil positioned 1-mm laterally off-center within the drift electric field region, as shown in Fig. 5. As a result, a minimum distance of approximately 20–21 mm, perpendicular to the foil surface, exists between the foil surface and the perimeter of the drift electric field region. The perimeter of the drift electric field region is defined by the perimeter of the microstrip electrode.

As illustrated in Fig. 5, assuming reaction products with full energy are emitted into the backfill gas perpendicular to the foil surface, the alpha-particle energy will be fully absorbed within the drift electric

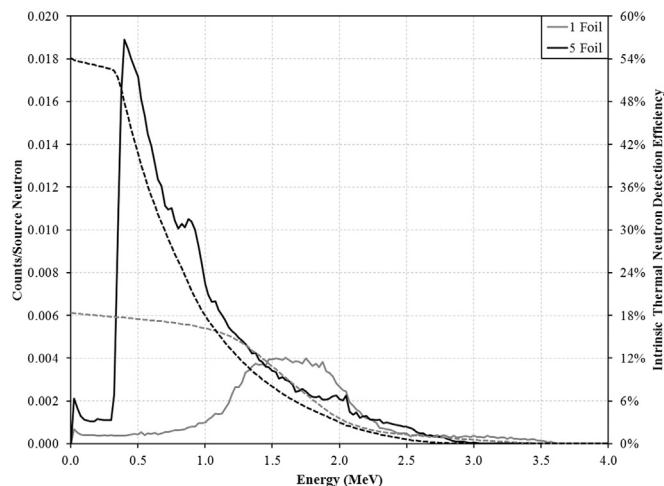


Fig. 4. MCNP6-simulated reaction-product pulse-height spectra (indicated by the left y-axis with units of counts/source neutron) for one (solid gray) and five (solid black) suspended ⁶Li foils contained within 10 psig (1.68 atm) of P-10 proportional gas. The dashed gray and black lines illustrate the change of ϵ_{th} as a function of LLD setting for one and five suspended ⁶Li foils, respectively. As the LLD setting is increased, the ϵ_{th} reduces as a function of the prominence of the reaction-product spectral features.

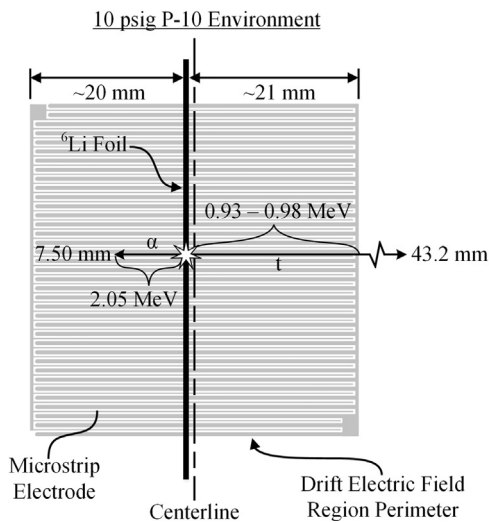


Fig. 5. Top-down view of the MCNP6 simulation environment for the single-foil ⁶Li-based SFMND showing the foil positioned 1-mm laterally off-center in the drift electric field region.

field region, while approximately 0.93–0.98 MeV of the triton energy is absorbed within the drift electric field region for ionization distances ranging from approximately 20 to 21 mm, respectively (Ziegler and Biersack, 2013). However, before reaction products escape the foil and enter the backfill gas, a distribution of reaction-product energy is lost due to self-absorption of the reaction products within the foil depending on the trajectory and site of creation of the reaction products relative to the foil surface. Assuming the reaction product is not absorbed by other solid structures or escapes the drift electric field region, the amount of energy deposited within the P-10 gas increases as the polar and/or azimuthal angle of emission deviates from perpendicular to the foil surface. Therefore, the amount of reaction-product energy deposited within the P-10 gas is a distribution that is dependent on the site of creation within the foil and the trajectory of the reaction products in both the foil and the P-10 gas.

Fig. 6 depicts the five-foil scenario, which was simulated with a spacing of 5.73 mm between neighboring foils. Again, assuming the full energy of the reaction products are emitted into the backfill gas

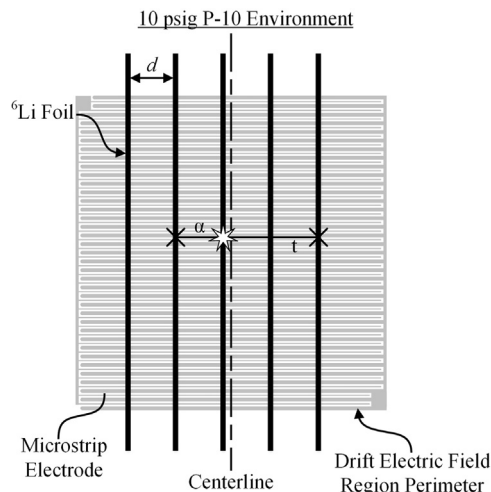


Fig. 6. Top-down view of the five-foil simulation scenario showing the positions of the five foils relative to the drift electric field region perimeter. The distance, d , between neighboring foils is 5.73 mm. Alpha particles emitted from interior foils undergo self-absorption upon entering a neighboring foil, indicated by a X. Tritons are capable of traveling through adjacent foils before undergoing self-absorption within a foil or escaping the drift electric field region perimeter.

perpendicular to the foil surface (both polar and azimuthal), the foil spacing allows for approximately 1.68 MeV and 0.25 MeV energy deposition of the alpha particles and tritons, respectively, to be absorbed within the backfill gas between neighboring foils (Ziegler and Biersack, 2013). For sufficiently-thin foils, the tritons are capable of ionizing the backfill gas between multiple foils by passing through one or more foils before eventually being absorbed in a foil or the chamber wall. The amount of energy deposited between neighboring foils increases as the polar and/or azimuthal angle of emission changes from perpendicular to the foil surface; however, the amount of energy lost from self-absorption within neighboring foils also increases for these trajectories. Thus, the distribution probability in the pulse-height spectrum decreases with energy deposition for the five-foil device compared to the single-foil device.

3. SFMND fabrication and testing

One- and five-foil ⁶Li-based SFMNDs were fabricated using Schott Borofloat® 33 microstrip electrodes (Edwards et al., 2018) at the Kansas State University Semiconductor Materials and Radiological Technologies (S.M.A.R.T.) Laboratory. 75- μ m thick, 96%-enriched ⁶Li foils, with approximate dimensions of 5.00 cm x 2.95 cm, were individually laminated to 0.79-mm (1/32 in.) thick aluminum frames to allow the non-laminated face of the ⁶Li foil to be uniformly-capable of allowing reaction products to escape the foil and enter the backfilled gas. Shown in Fig. 7 are the front (top left) and back (top right) of a ⁶Li-laminated aluminum frame. Each aluminum frame contained an opening in the center, with approximate dimensions of 4.45 cm x 2.54 cm, to allow reaction products to escape from either side of the laminated-⁶Li foil. The laminated frames were then positioned within a 4.3 cm x 5.9 cm x 3.4 cm 3D-printed support device containing twenty 1-mm wide frame slots. The frame slots were separated from one another by 1-mm thick dividers. Although the 3D-printed support device contained twenty frame slots, devices with only one or five suspended foils were fabricated and tested. The position of the single foil within the 3D-printed support device was offset from center by 1 mm and the five foils were spaced 5.73 mm apart from one another. Also shown in Fig. 7 are the 3D-printed support devices containing one (bottom left) and five (bottom right) ⁶Li-laminated aluminum frames.

The 3D-printed support device was positioned between a Schott Borofloat® 33 microstrip electrode and a planar, drift electrode as



Fig. 7. (Top left) Front of a 0.79-mm (1/32 in.) thick aluminum frame with a laminated ${}^6\text{Li}$ foil adhered to the surface. The entire face of the laminated ${}^6\text{Li}$ foil is capable of allowing reaction products to escape the ${}^6\text{Li}$ foil and enter the detector gas. (Top right) Backside of an aluminum frame showing that only the center opening of the frame allows reaction products to escape the ${}^6\text{Li}$ foil and enter the detector gas. 3D-printed plastic support device containing one (bottom left) and five (bottom right) ${}^6\text{Li}$ foils used for suspending ${}^6\text{Li}$ foil(s) between microstrip and drift electrodes.

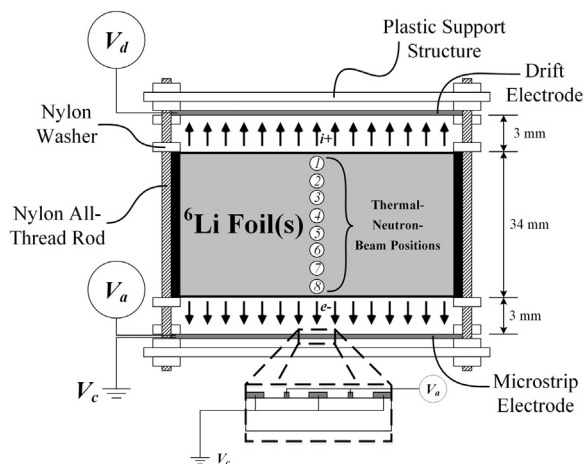


Fig. 8. Illustration of the SFMND showing the ${}^6\text{Li}$ foil(s) orientation relative to the microstrip and drift electrodes. The eight thermal-neutron beam positions are indicated by numbered circles.

illustrated in Fig. 8. The fabrication and characterization of the 4.2 cm \times 4.2 cm Schott Borofloat[®] 33 microstrip electrode containing 25- μm wide anode strips and 500- μm wide cathode strips with an anode-to-anode pitch of 1000 μm is documented in a separate report (Edwards et al., 2018). A plastic support structure was used to maintain the positions and vertical alignment of the electrodes and the ABS plastic 3D-printed support device throughout the duration of testing. The entire testing assembly was positioned within a sealed aluminum enclosure that was pressurized with 10.0 psig (1.68 atm) of P-10 proportional gas. Prior to conducting ϵ_{th} measurements, the sealed test enclosure was maintained under rough vacuum overnight and surrounded by heat tape to perform a bake-out procedure in an attempt to remove moisture and other volatiles.

Measurements of ϵ_{th} were conducted using the diffracted neutron beam of the Kansas State University TRIGA Mk II research reactor at a reactor power level of 100 kW_{th} . A cadmium collimator was used with a

2.5 mm diameter aperture. Measurements of ϵ_{th} were performed for eight discrete thermal-neutron beam positions, in 3.18-mm increments, along the length of the ${}^6\text{Li}$ foil(s) starting from the highest position (position 1), closest to the drift electrode surface, and ending at the lowest position (position 8), closest to the microstrip electrode surface (Fig. 8). The ϵ_{th} at each thermal-neutron beam position was calculated in reference to a 4.0 atm, 5.08-cm diameter, 15.24-cm long Reuter Stokes ${}^3\text{He}$ tube with an ϵ_{th} of $80.7 \pm 0.5\%$ (McGregor et al., 2009; McGregor and Shultis, 2011). The pressure of the P-10 proportional gas of 10.0 psig (1.68 atm) contained within the sealed aluminum enclosure was monitored throughout the duration of the ϵ_{th} measurements. The cathode strips were maintained at ground potential for all SFMND measurements. The anode-strip operating voltage, V_a , was set at 300 V and 370 V for the single- and five-foil devices, respectively, and the drift electrode voltage, V_d , was set at -1212 V and -1141 V, respectively, in order to maintain a reduced electric field strength of approximately $0.3 \text{ V cm}^{-1} \text{ Torr}^{-1}$ (Knoll, 2010). The operating voltage of the anode strips for the five-foil measurements was increased above that of the one-foil measurements to increase the gas multiplication factor. This was necessary due to the reduction in energy deposition relative to the one-foil device (predicted from the simulated reaction product spectra in Fig. 4).

The gamma rejection ratio (GRR) was calculated for the one- and five-foil devices for a ${}^{137}\text{Cs}$ exposure rate of 50 mR h^{-1} using Eqs. (2) and (3) (Nelson, 2013; Wilson et al., 2011),

$$GRR = \frac{\left(\frac{CTS_\gamma}{t_\gamma}\right) - \left(\frac{CTS_{Background}}{t_{Background}}\right)}{A \cdot BR \cdot \Omega_f}, \quad (2)$$

where BR is the branching ratio, A is the source activity, and Ω_f is the fractional solid angle.

$$\Omega_f = \frac{1}{\pi} \arctan \left[\frac{W \times L}{4 \times D \times \sqrt{\frac{W^2}{4} + \frac{L^2}{4} + D^2}} \right]. \quad (3)$$

CTS_γ and $CTS_{Background}$ are the measured total gross counts for the

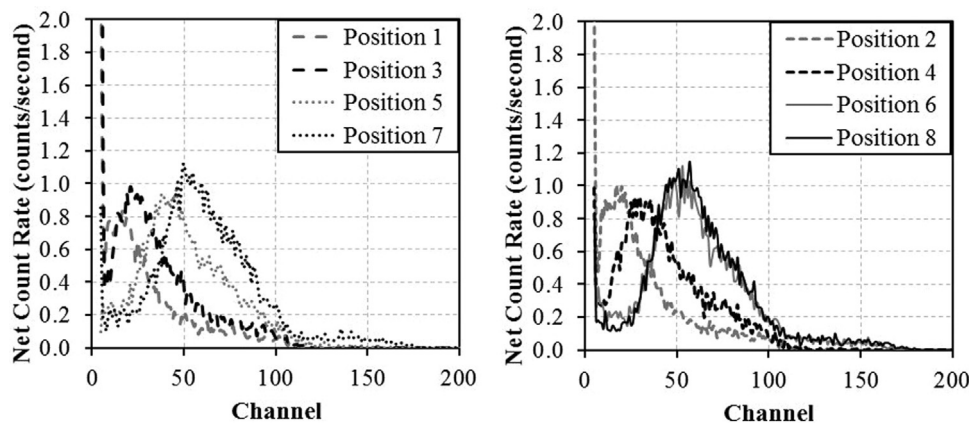


Fig. 9. Measured reaction-product pulse-height spectra for eight discrete thermal-neutron beam positions incident on a single 75- μm thick ^6Li foil contained within a sealed aluminum enclosure pressurized with 10 psig (1.68 atm) of P-10 proportional gas. The measured spectra are plotted on two graphs for clarity of the individual reaction-product pulse-height spectra.

^{137}Cs source and background measurements, respectively, and t_s and $t_{\text{Background}}$ are the ^{137}Cs source and background measurement times, respectively. The corrected activity of the ^{137}Cs was 62.76 mCi with a known ^{137}Cs branching ratio of 0.85 for 661.7 keV gamma rays. The fractional solid angle, Ω_f , was defined for a square-aperture device of a specified width, W , and length, L , for a source positioned at distance, D , from the device aperture. The operating voltages used for performing the GRR measurements were the same for those used for measuring the ϵ_{th} distributions. The GRR error, σ_{GRR} , was defined as

$$\sigma_{GRR} = \sqrt{\left(\frac{\partial GRR}{\partial CTS_\gamma}\right)^2 \sigma_{CTS_\gamma}^2 + \left(\frac{\partial GRR}{\partial CTS_{\text{Background}}}\right)^2 \sigma_{CTS_{\text{Background}}}^2}, \quad (4)$$

based on the counting errors of the ^{137}Cs and background measurements, σ_{CTS_γ} and $\sigma_{CTS_{\text{Background}}}$, respectively.

4. Results and discussion

Shown in Fig. 9 are the reaction-product pulse-height spectra measured using a one-foil ^6Li -based SFMND for eight discrete thermal-neutron beam positions. A down-shift in spectral features to lower channel numbers occurred as the thermal-neutron beam was positioned further from the microstrip electrode surface. This shift in spectral features is consistent with the drift electric field strength distribution measurements conducted using a collimated ^{241}Am alpha-particle source described in a separate report (Edwards et al., 2018). As a result of the down-shift in spectral features, a non-uniform distribution of ϵ_{th} was measured as the thermal-neutron beam was positioned further away from the microstrip electrode surface (depicted in Fig. 10 and listed in Table 1).

A maximum ϵ_{th} of $12.58 \pm 0.15\%$ was measured for a non-zero LLD setting at position 8, the closest thermal-neutron beam position to the microstrip electrode surface. The maximum measured ϵ_{th} for a one-foil ^6Li -based SFMND was lower than the expected ϵ_{th} of 18.36% predicted from MCNP6 simulations. It is suspected that the lower measured ϵ_{th} is a consequence of combined effects, including electron attachment, a non-uniform electric field distribution, and the signal-to-noise ratio of the readout electrode system (arising from the measured microstrip electrode capacitance of 67 pF (Edwards et al., 2018)). The use of ABS plastic, nylon, and other high-outgassing materials to construct the 3D-printed support device and other components may introduce contaminants that promote electron attachment, and it is suspected such contamination may be the cause of the ϵ_{th} degradation as the thermal-neutron beam was positioned further away from the microstrip electrode surface. The non-uniform distribution of pulse-amplitudes previously measured using a collimated ^{241}Am alpha-particle source for a similar electrode setup (described in a separate report (Edwards et al.,

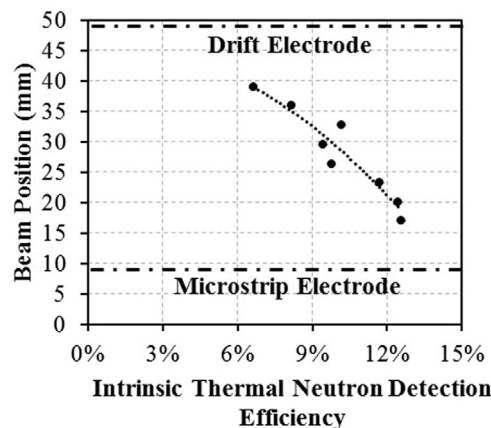


Fig. 10. Measured ϵ_{th} as a function of the position of the thermal-neutron beam for a one-foil ^6Li -based SFMND.

Table 1

Measured ϵ_{th} of a SFMND containing one ^6Li foil suspended in 10 psig (1.68 atm) of P-10 proportional gas. Data for eight discrete thermal-neutron beam positions along the length of the ^6Li foil between the microstrip and drift electrodes are tabulated.

Position	Beam Height Above Microstrip Surface (mm)	Measured Intrinsic Thermal Neutron Detection Efficiency, ϵ_{th}
1	30.6	$6.63 \pm 0.12\%$
2	27.4	$8.16 \pm 0.13\%$
3	24.2	$10.17 \pm 0.14\%$
4	21.0	$9.44 \pm 0.14\%$
5	17.9	$9.77 \pm 0.14\%$
6	14.7	$11.71 \pm 0.14\%$
7	11.5	$12.45 \pm 0.15\%$
8	8.5	$12.58 \pm 0.15\%$

2018)) is consistent with the non-uniform distribution of measured ϵ_{th} . Thus, a second suspected cause for the non-uniform distribution of measured ϵ_{th} is a non-uniform electric field distribution. A non-uniform electric field distribution would result in a distribution of charge-carrier velocities, position dependent between the microstrip and drift electrodes, resulting in a non-uniform distribution of measured pulse amplitudes. The implementation of a Frisch grid (see description in Knoll (2010)) between the microstrip electrode and the bottom of the foil(s) should produce a uniform electric field region where the foils are positioned, thus allowing for a more uniform distribution of the measured ϵ_{th} . Finally, the third suspected cause is attributed to the microstrip electrode capacitance. A reduction in microstrip electrode capacitance should further increase the signal-to-noise ratio, allowing for separation

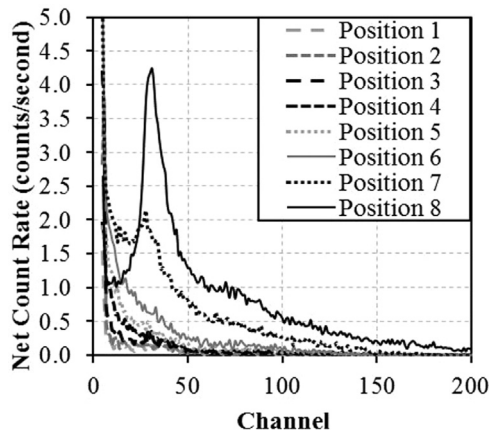


Fig. 11. Measured reaction-product pulse-height spectra for eight discrete thermal-neutron beam positions incident on five 75- μm thick ${}^6\text{Li}$ foils contained within a sealed aluminum enclosure pressurized with 10 psig (1.68 atm) of P-10 proportional gas. The spectral features diminished more rapidly compared to the one-foil case (see discussion in text).

of low-energy events from electronic noise and therefore further increasing the measured ϵ_{th} .

Shown in Fig. 11 are the reaction-product pulse-height spectra as a function of thermal-neutron beam position for the five-foil ${}^6\text{Li}$ -based SFMND. Similar to the one-foil ${}^6\text{Li}$ -based SFMND, a down-shift in spectral features occurred as the thermal-neutron beam was positioned further away from the microstrip electrode surface. However, the measured ϵ_{th} shown in Fig. 12 and listed in Table 2, rapidly decreased as the thermal-neutron beam was positioned further away from the microstrip electrode surface compared to the distribution of ϵ_{th} measured with the one-foil ${}^6\text{Li}$ -based SFMND. Recalling the simulated reaction-product pulse-height spectra in Fig. 4, the spectral features for a five-foil ${}^6\text{Li}$ -based SFMND are most prominent in lower energy bins between 300 and 1000 keV. In comparison, the simulated reaction-product pulse-height spectrum of a one-foil ${}^6\text{Li}$ -based SFMND contains the most prominent spectral features between energies of approximately 1.2 – 2.2 MeV. It is suspected that the ϵ_{th} degraded more rapidly for the five-foil ${}^6\text{Li}$ -based SFMND compared to the one-foil ${}^6\text{Li}$ -based SFMND due to the lower-energy pulse-height spectral features coupled with suspected problems attributed to electronic noise, electron attachment, non-uniform electric field strength distribution, or any combination thereof. The maximum ϵ_{th} was measured at position 8 for a non-zero LLD setting and was calculated to be $29.75 \pm 0.26\%$. This measured ϵ_{th} was significantly lower than the theoretical ϵ_{th} of 54.08% simulated with MCNP6.

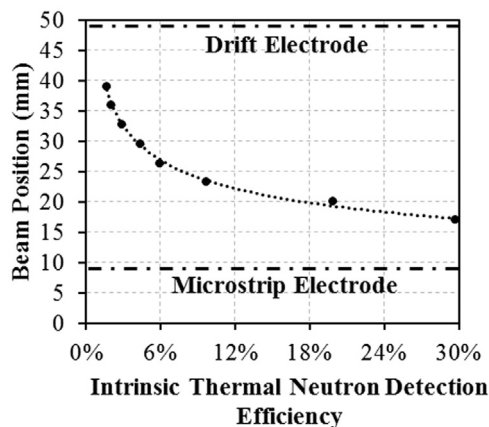


Fig. 12. Measured ϵ_{th} as a function of the thermal-neutron beam position for a five-foil ${}^6\text{Li}$ -based SFMND. The ϵ_{th} decreased more rapidly as the thermal-neutron beam was positioned further away from the microstrip electrode surface compared to the one-foil case.

Table 2

Measured ϵ_{th} of a SFMND containing five suspended ${}^6\text{Li}$ foils using 10 psig (1.68 atm) of P-10 proportional gas for eight discrete thermal-neutron beam positions along the length of the ${}^6\text{Li}$ foil between the microstrip and drift electrodes.

Position	Beam Height Above Microstrip Surface (mm)	Measured Intrinsic Thermal Neutron Detection Efficiency, ϵ_{th}
1	30.6	$1.65 \pm 0.09\%$
2	27.4	$2.07 \pm 0.09\%$
3	24.2	$2.95 \pm 0.10\%$
4	21.0	$4.43 \pm 0.10\%$
5	17.9	$5.95 \pm 0.11\%$
6	14.7	$9.69 \pm 0.11\%$
7	11.5	$19.92 \pm 0.19\%$
8	8.5	$29.75 \pm 0.26\%$

A comparison was performed by summing the reaction-product pulse-height spectra from the eight discrete thermal-neutron beam positional measurements using the five-foil ${}^6\text{Li}$ -based SFMND, shown in Fig. 11, and normalizing the net count rate about the most prominent spectral feature. A second, isolated measurement was conducted using the five-foil ${}^6\text{Li}$ -based SFMND exposed to a 22-ng ${}^{252}\text{Cf}$ source surrounded by an ANSI-specified moderator cask (American National Standards Institute, 2013) and again the net count rate was normalized about the most prominent spectral feature. The two sets of data were plotted and compared as shown in Fig. 13 and possess similar spectral features. The ${}^{252}\text{Cf}$ data depicts a higher prominence of spectral features in the lower channels below the prominent spectral feature approximately located at channel 30. The elevated count rate in lower channels occurred because the ${}^{252}\text{Cf}$ measurement includes a nearly uniform distribution of neutron-interaction locations along the length of the foil from the uncollimated ${}^{252}\text{Cf}$ source and moderator cask. If additional thermal-neutron beam measurements were performed for beam positions between the reported positions, it is expected that the spectral features would be closer matched.

The one- and five-foil GRRs were calculated to be $6.46 \times 10^{-5} \pm 4.32 \times 10^{-7}$ and $7.96 \times 10^{-5} \pm 4.65 \times 10^{-7}$, respectively, for a ${}^{137}\text{Cs}$ exposure rate of 50 mR h^{-1} . The difference between the GRR values measured in the present work and lower values previously reported for Li-Foil MWPCs (Nelson, 2013; Nelson et al., 2014a) is suspected to be a consequence of the aluminum wall thickness (0.9525 cm) of the sealed test enclosure. The amount of aluminum in the test enclosure, compared to thinner-walled enclosures previously used for fabricating and testing Li-foil MWPCs (Nelson, 2013; Nelson et al., 2014a), results in an increase in measured ${}^{137}\text{Cs}$ counts from gamma rays scattering off of the enclosure walls (Berger et al., 2010). Future measurements will be performed using thinner-walled aluminum enclosures ($\leq 0.3175 \text{ cm}$).

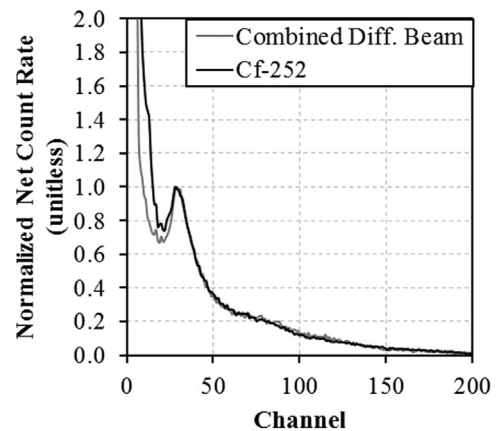


Fig. 13. Normalized comparison of the summed spectra of Fig. 11 to that of an uncollimated, moderated ${}^{252}\text{Cf}$ neutron source.

5. Conclusions

Non-uniform ε_{th} distributions were measured for discrete thermal-neutron beam positions using one- and five-foil ${}^6\text{Li}$ -based SFMNDs. The maximum measured ε_{th} for one- and five-foil ${}^6\text{Li}$ -based SFMNDs were $12.58 \pm 0.15\%$ and $29.75 \pm 0.26\%$, respectively, both lower than the MCNP6-simulated values of 18.36% and 54.08%, respectively. Although the cause of the deviation between simulated and measured ε_{th} is uncertain, electron attachment is suspected to be occurring within the drift electric field region. The significance of electron attachment, if any, will be explored by replacing all high-outgassing materials contained within the sealed aluminum test enclosure with low-outgassing materials. Additionally, the non-uniform distribution of measured ε_{th} is suspected to occur due to a non-uniform electric field distribution. The addition of a Frisch grid between the microstrip electrode and the bottom of the foil(s) should produce a uniform electric field distribution, thus allowing for a more uniform distribution of measured ε_{th} . Finally, the signal-to-noise ratio may be further improved by utilizing a microstrip electrode with a lower capacitance than the Schott Borofloat® 33 microstrip electrode (measured to be 67 pF (Edwards et al., 2018)) that was used in the present work. An increase in signal-to-noise ratio should further increase the measured ε_{th} by separating more low-energy events from electronic noise. *GRRs* of $6.46 \times 10^{-5} \pm 4.32 \times 10^{-7}$ and $7.96 \times 10^{-5} \pm 4.65 \times 10^{-7}$ were measured using one- and five-foil ${}^6\text{Li}$ -based SFMNDs, respectively, for a ${}^{137}\text{Cs}$ exposure rate of 50 mR h^{-1} . The wall-thickness of the sealed aluminum enclosure is suspected to cause higher measured *GRRs*, relative to previously-measured *GRRs* using Li-foil MWPCs (Nelson, 2013; Nelson et al., 2014a), and thus the enclosure wall-thickness will be reduced for future testing efforts in an attempt to improve the *GRR*.

Acknowledgements

SFMNDs were fabricated and characterized at the Kansas State University Semiconductor Materials and Radiological Technologies (S.M.A.R.T.) Laboratory (Manhattan, KS). Thermal-neutron measurements were performed at the Kansas State University TRIGA Mark II nuclear reactor. The authors wish to express their gratitude to the KSU TRIGA Mark II nuclear reactor staff for the assistance provided during testing.

References

- Kouzes, R.T., 2009. The ${}^3\text{He}$ Supply Problem. Pacific Northwest National Laboratory, Richland, WA.
- Shea, D.A., Morgan, D., 2010. "The Helium-3 Shortage: Supply, Demand, and Options for Congress," in ed., by CRS Reports for Congress.
- Kouzes, R.T., Ely, J.H., Erikson, L.E., et al., 2010. Neutron detection alternatives to ${}^3\text{He}$ for national security applications. *Nucl. Instrum. Methods A* 623 (3), 1035–1045.
- Hurd, A.J., Kouzes, R.T., 2014. Why new neutron detector materials must replace helium-3. *Eur. Phys. J. Plus* 129 (10), 1–3.
- Kouzes, R.T., Lintereur, A.T., Siciliano, E.R., 2015. Progress in alternative neutron detection to address the helium-3 shortage. *Nucl. Instrum. Methods A* 784, 172–175.
- Nelson, K.A., Bellinger, S.L., Montag, B.W., 2011. *et al.*, "Investigation of aerogel, saturated foam, and foil for thermal neutron detection, In: Proceedings of Nuclear Science Symposium and Medical Imaging Conference (NSS/MIC), 2011 IEEE, pp. 1026–1029, 23–29 Oct, 2011.
- Nelson, K.A., Bellinger, S.L., Montag, B.W., et al., 2012. Investigation of a lithium foil multi-wire proportional counter for potential ${}^3\text{He}$ replacement. *Nucl. Instrum. Methods A* 669, 79–84.
- Nelson, K.A., 2013. An Investigation of Aerogels, Foams, and Foils for Multi-Wire Proportional Counter Neutron Detectors, Doctorate, Mechanical and Nuclear Engineering, Kansas State University.
- Nelson, K.A., Kusner, M.R., Montag, B.W., et al., 2014a. Characterization of a mid-sized Li foil multi-wire proportional counter neutron detector. *Nucl. Instrum. Methods A* 762, 119–124.
- Nelson, K.A., Hinson, N.J., Kusner, M.R., 2014b. *et al.*, Results and potential applications of handheld, mid-sized, and large-area low-cost Li foil MWPCS, In: Proceedings of IEEE Nuclear Science Symposium and Medical Imaging Conference (NSS/MIC), pp. 1–5, 8–15 Nov. 2014.
- Nelson, K.A., Edwards, N.S., Kusner, M.R., et al., 2015. A modular large-area lithium foil multi-wire proportional counter neutron detector. *Radiat. Phys. Chem.* 116, 165–169.
- Edwards, N.S., Montag, B.W., Henson, L.C., 2016. *et al.*, "Lithium foil gas-filled neutron detector using microstrip electrodes," In: Proceedings of IEEE Nuclear Science Symposium and Medical Imaging Conference (NSS/MIC), pp. 1–3, Oct. 29 2016–Nov. 5, 2016.
- Oed, A., 1988. Position-sensitive detector with microstrip anode for electron multiplication with gases. *Nucl. Instrum. Methods A* 263 (2), 351–359.
- Oed, A., Convert, P., Berneron, M., et al., 1989. A new position sensitive proportional counter with microstrip anode for neutron detection. *Nucl. Instrum. Methods A* 284 (1), 223–226.
- Vellettaz, N., Assaf, J.E., Oed, A., 1997. Two-dimensional gaseous microstrip detector for thermal neutrons. *Nucl. Instrum. Methods A* 392 (1–3), 73–79.
- Clergeau, J.F., Convert, P., Feltin, D., et al., 2001. Operation of sealed microstrip gas chambers at the ILL. *Nucl. Instrum. Methods A* 471 (1–2), 60–68.
- Takahashi, H., Siritiprussamee, P., Kai, M., et al., 2004. Development of a two-dimensional multi-grid-type microstrip gas chamber for spallation neutron source. *Nucl. Instrum. Methods A* 529 (1–3), 348–353.
- Fujita, K., Takahashi, H., Siritiprussamee, P., et al., 2007. A high-resolution two-dimensional ${}^3\text{He}$ neutron MSGC with pads for neutron scattering experiments. *Nucl. Instrum. Methods A* 580 (2), 1027–1030.
- Bateman, J.E., Dalgliesh, R.M., Duxbury, D.M., et al., 2010. The FastGas detector. *Nucl. Instrum. Methods A* 616 (1), 59–64.
- Bateman, J.E., Dalgliesh, R., Duxbury, D.M., et al., 2013. The OSMOND detector. *Nucl. Instrum. Methods A* 698, 168–176.
- Oed, A., 2004. Detectors for thermal neutrons. *Nucl. Instrum. Methods A* 525 (1–2), 62–68.
- Gebauer, B., Schulz, C., Wilpert, T., et al., 1998. Large-area low-pressure microstrip gas chambers for thermal neutron imaging. *Nucl. Instrum. Methods A* 409 (1–3), 56–62.
- Masaoka, S., Nakamura, T., Yamagishi, H., et al., 2003. Optimization of a micro-strip gas chamber as a two-dimensional neutron detector using gadolinium converter. *Nucl. Instrum. Methods A* 513 (3), 538–549.
- Edwards, N.S., Montag, B.W., Henson, L.C., et al., 2018. Fabrication and characterization of Schott Borofloat® 33 microstrip electrodes. *Radiat. Phys. Chem.* (Submitted).
- Knoll, G.F., 2010. Radiation Detection and Measurement, 4th ed. John Wiley & Sons, Inc, Hoboken, NJ.
- Tsoufanidis, N., 1995. Measurement and Detection of Radiation, 2nd ed. Taylor & Francis, Washington, DC.
- McGregor, D.S., Hammig, M.D., Yang, Y.H., et al., 2003. Design considerations for thin film coated semiconductor thermal neutron detectors—I: basics regarding alpha particle emitting neutron reactive films. *Nucl. Instrum. Methods A* 500 (1–3), 272–308.
- Ziegler, J.F., Biersack, J.P., 2013. SRIM-2013 Code, <<http://www.srim.org/>>.
- McGregor, D.S., McNeil, W.J., Bellinger, S.L., et al., 2009. Microstructured semiconductor neutron detectors. *Nucl. Instrum. Methods A* 608 (1), 125–131.
- McGregor, D.S., Shultis, J. Kenneth, 2011. Reporting detection efficiency for semiconductor neutron detectors: a need for a standard. *Nucl. Instrum. Methods A* 632 (1), 167–174.
- Wilson, L., Duraj, A., Kusner, M., 2011. "Neutron Detection for Portal Monitors Performance Evaluation," in ed., by Saint-Gobain Crystals Scintillation Products, Saint Gobain Ceramics & Plastics, Inc., Scintillation Products Technical Note.
- American National Standards Institute, 2013. "American National Standard Performance Criteria for Backpack-Based Radiation-Detection Systems Used for Homeland Security," in ANSI N42.53-2013, ed., by The Institute of Electrical and Electronics Engineers, Inc., pp. 1–62.
- Berger, M.J., Hubbell, J.H., Seltzer, S.M., 2010. *et al.*, "XCOM: Photon Cross Section Database (version 1.5)," in ed., by.